

A Template-Based Search for Large-Scale-Structure–Correlated Anisotropy in the Nanohertz Gravitational-Wave Background Using the Public NANOGrav 15-Year Data Set

YUN FANG^{1,2}

¹*Institute of Fundamental Physics and Quantum Technology, Ningbo University, Ningbo, 315211, China*

²*School of Physical Science and Technology, Ningbo University, Ningbo, 315211, China*

(Dated: March 3, 2026)

ABSTRACT

Recent PTA analyses reporting evidence for a nanohertz common-spectrum process motivate targeted tests of whether any anisotropic component of the stochastic gravitational-wave background (SGWB) is correlated with the nearby large-scale structure (LSS), as anticipated for an astrophysical background dominated by supermassive black hole binaries. We present the first Bayesian PTA likelihood analysis that embeds an externally observed, full-sky galaxy-survey LSS template directly as an overlap-reduction-function (ORF) component. Using the 2MASS Photometric Redshift (2MPZ) galaxy catalog, we construct low-multipole LSS–correlated ORF templates in two redshift slices ($0 < z \leq 0.1$ and $0.1 < z \leq 0.2$) and model PTA cross-correlations as $\Gamma_{ab} = \Gamma_{ab}^{\text{HD}} + \sum_i \epsilon_i \Gamma_{ab}^{\text{LSS}(i)}$, where ϵ_i quantifies the amplitude of an SGWB component whose angular correlations project onto the fixed 2MPZ LSS templates. Applying this framework to the NANOGrav 15-year dataset, we find no statistically significant evidence for an LSS-correlated component: ϵ_i is consistent with zero in both single-bin and two-bin analyses (e.g., $\epsilon_1 = 0.20_{-1.66}^{+1.68}$ and $\epsilon_2 = -0.11_{-1.83}^{+2.04}$; 68% credible intervals), and Bayes factors favor the isotropic Hellings–Downs hypothesis ($\mathcal{B}_{\text{HD}+\text{LSS}_1, \text{HD}} = 0.40$, $\mathcal{B}_{\text{HD}+\text{LSS}_2, \text{HD}} = 0.43$, $\mathcal{B}_{\text{HD}+\text{LSS}_{1+2}, \text{HD}} = 0.11$). We therefore place upper limits on any 2MPZ-traced, LSS-correlated contribution to the SGWB at $z < 0.2$. More broadly, our framework provides a reproducible pathway for incorporating observed LSS information into PTA anisotropy searches and naturally motivates extensions to finer redshift tomography and next-generation PTA datasets.

Keywords: gravitational waves — pulsars: general — methods: data analysis — cosmology: observations — large-scale structure of universe

1. INTRODUCTION

Pulsar timing arrays (PTAs) use precision timing of an ensemble of millisecond pulsars to probe gravitational waves (GWs) in the nanohertz band, enabling searches for both a stochastic gravitational-wave background (SGWB) and individually resolvable sources (Sazhin 1978; Detweiler 1979; Foster & Backer 1990; Creighton & Anderson 2011; Maggiore 2008). A global PTA effort is now in place, including the Parkes PTA (PPTA)(Manchester 2013; Reardon et al. 2023), the European PTA (EPTA)(Kramer & Champion 2013; EPTA Collaboration et al. 2023), the North American Nanohertz Observatory for Gravitational Waves

(NANOGrav)(McLaughlin 2013; Agazie et al. 2023a), the Indian PTA (InPTA)(Joshi et al. 2018; EPTA Collaboration et al. 2023), the Chinese PTA (CPTA)(Nan et al. 2011; Smits et al. 2009; Xu et al. 2023), and the MeerKAT PTA (MPTA)(Miles et al. 2023). By combining data and expertise through the International PTA (IPTA)(Manchester & IPTA 2013; Verbiest et al. 2016; Perera et al. 2019) and looking ahead to next-generation facilities such as the Square Kilometre Array (e.g., Lazio 2013; Wang & Mohanty 2017), PTAs are entering an era in which the SGWB is becoming accessible to detailed characterization (e.g., Agazie et al. 2023a; EPTA Collaboration et al. 2023; Agazie et al. 2023). Recent analyses by CPTA, NANOGrav, EPTA(+InPTA), and PPTA report evidence for a nanohertz common-spectrum process with spatial correlations consistent with a GW back-

ground (Xu et al. 2023; Agazie et al. 2023a; Reardon et al. 2023; EPTA Collaboration et al. 2023).

With accumulating evidence for a nanohertz common-spectrum process, a central question is its physical origin. Different source classes predict distinct spatial statistics for the SGWB, making anisotropy a powerful complement to spectral characterization (e.g., Taylor & Gair 2013; Cornish & van Haasteren 2014; Mingarelli et al. 2017; Hotinli et al. 2019; Agazie et al. 2023). The interpretation most often discussed is an SGWB produced by the cosmic population of inspiralling supermassive black hole binaries (SMBHBs) (e.g., Phinney 2001; Jaffe & Backer 2003; Sesana 2013; Agazie et al. 2023; Bi et al. 2023), while alternative early-Universe mechanisms (e.g., cosmic defects or phase transitions) remain viable given current uncertainties (e.g., Kosowsky et al. 1992; Caprini & Figueroa 2018; Ellis & Lewicki 2021; Afzal et al. 2023). To distinguish these possibilities, it is essential to go beyond an isotropic characterization and test whether the SGWB exhibits spatial statistics that are characteristic of its origin.

Anisotropy and its correlation with the large-scale structure (LSS) provide a particularly direct discriminant. If a significant fraction of the PTA-band SGWB is sourced by SMBHBs, departures from statistical isotropy are generically expected because the signal is weighted toward low redshifts where galaxies and dark-matter haloes are clustered. This links the SGWB anisotropy to the cosmic web: SMBHBs co-evolve with their host galaxies and trace the assembly history of dark-matter haloes, as suggested by SMBH–galaxy and SMBH–halo scaling relations (e.g., Ferrarese & Merritt 2000; Gebhardt et al. 2000; Kormendy & Ho 2013; Reines & Volonteri 2015; Matthee et al. 2025), and AGNs preferentially reside in massive haloes and overdense environments (e.g., Wake et al. 2008; Donoso et al. 2010; Hickox et al. 2011; Hashiguchi et al. 2023). In addition, because the nanohertz SGWB is built from a finite number of binaries, Poisson fluctuations in the number and sky distribution of contributing systems generate a “shot-noise” anisotropy component (e.g., Ravi et al. 2012; Cornish & Sesana 2013; Allen et al. 2024), superposed on any LSS-driven modulation. By contrast, many early-Universe mechanisms predict SGWBs that are statistically isotropic at leading order, with only small departures from isotropy expected (e.g., Chiara Guzzetti et al. 2016; Taylor & Gair 2013; Alba & Maldacena 2016; Caprini & Figueroa 2018; Bartolo et al. 2020). Characterizing SGWB anisotropy therefore provides a complementary probe for distinguishing astrophysical and cosmological interpretations of the signal (e.g., Mingarelli et al. 2013; Taylor & Gair 2013;

Cornish & van Haasteren 2014; Hotinli et al. 2019; Agazie et al. 2023).

A substantial literature has developed the theoretical and data-analysis foundations for PTA anisotropy. Early work introduced multipolar descriptions of the GW power distribution on the sky and generalized overlap-reduction functions (ORFs) for anisotropic PTA cross-correlations (Mingarelli et al. 2013; Gair et al. 2014), and developed Bayesian search pipelines to infer angular structure in simulated PTA data (Taylor & Gair 2013). Dedicated searches on real PTA data have reconstructed the GW sky using model-independent spherical-harmonic and map-based methods and, despite occasional low-significance hotspots, have found no statistically significant anisotropy beyond the monopole, placing upper limits on low- ℓ power (e.g., Taylor et al. 2015; Agazie et al. 2023; Grunthal et al. 2024; Chen et al. 2026). A practical complication is that realistic nanohertz SGWBs are subject to large realization scatter (“cosmic variance”) from a finite population of SMBHBs, in which a few bright binaries can produce a “bumpy” GW sky and potentially mask more specific clustering signatures (e.g., Taylor et al. 2020; Bécsy et al. 2022; Konstandin et al. 2025). At the same time, recent methodological work emphasizes that sensitivity can improve when information from multiple anisotropy modes is combined optimally, motivating low-dimensional, physically grounded anisotropy models in the low-SNR regime (e.g., Hotinli et al. 2019; Ali-Haïmoud et al. 2021). In parallel, local-Universe galaxy catalogs and cosmological simulations have been used to predict anisotropic nanohertz GW “landscapes” and source clustering (e.g., Mingarelli et al. 2017; Sah et al. 2024; Yang et al. 2025), and to incorporate external astrophysical priors in targeted PTA searches (e.g., Arzoumanian et al. 2021). Recent work further shows that cross-correlations with galaxy maps can isolate the component that traces the underlying LSS and substantially improve detectability even in the presence of strong Poisson shot noise (e.g., Semenzato et al. 2024; Cusin et al. 2025).

In this work, we adopt a complementary, template-based strategy for testing SGWB anisotropy. We use the observed galaxy overdensity field to construct redshift-sliced, LSS-derived ORF templates, and model the PTA cross-correlation as a linear superposition of the isotropic HD form and an LSS-tracing contribution with mixing coefficients that are inferred directly from the NANOGrav 15 yr data (Agazie et al. 2023a,b). This framework enables an explicit test of the hypothesis that any anisotropic component of the PTA-band SGWB follows the angular distribution of matter in the nearby

Universe. Concretely, we employ the 2MASS Photometric Redshift (2MPZ) catalog (Bilicki et al. 2014) to build the LSS templates. While current Bayes factors prefer the isotropic model, the data nonetheless place upper limits on the LSS-correlated components. As a conservative first step, we restrict attention to $z < 0.2$ and relatively narrow redshift slices, enabling controlled validation of the LSS reconstruction and the resulting ORF templates.

This paper is organized as follows. In Section 2 we review the basic PTA response to an isotropic and anisotropic SGWB and define the corresponding ORFs. In Section 3 we motivate an LSS-informed anisotropy ansatz and derive the LSS-template ORF parameterization, leading to the binned mixed-ORF model. In Section 4 we describe the construction of redshift-sliced 2MPZ overdensity maps and our cut-sky MAP reconstruction of low- ℓ spherical-harmonic coefficients used to build the LSS ORF templates. In Section 5 we present Bayesian constraints from the NANOGrav 15-year dataset on single-bin and two-bin LSS-modulated ORF models and report hypermodel Bayes-factor comparisons against the HD-only hypothesis. We discuss the implications, limitations, and prospects for future PTA datasets in Section 6. Additional diagnostics of the low- ℓ reconstruction are provided in Appendix A.

2. BASIC CONCEPTS OF ISOTROPIC AND ANISOTROPIC ORF

In the weak-field, transverse-traceless (TT) gauge, the dimensionless metric perturbation can be expanded as

$$h_{ij}(t, \mathbf{x}) = \sum_{A=+, \times} \int df \int d\mathbf{n} h_A(f, \mathbf{n}) e^{2\pi i f(t - \mathbf{n} \cdot \mathbf{x})} e_{ij}^A(\mathbf{n}), \quad (1)$$

where e_{ij}^A is the polarization tensor and $h_A(f, \mathbf{n})$ is the amplitude of the GW propagate in direction \mathbf{n} with frequency f . The pulsar redshift z_a , for pulsar a located in direction \mathbf{p}_a , is given by (e.g., Detweiler 1979; Anholm et al. 2009; Gair et al. 2014)

$$z_a(t) = \sum_A \int df \int d\mathbf{n} F_a^A(\mathbf{n}) h_A(f, \mathbf{n}) e^{2\pi i f t} \times \left[1 - e^{-2\pi i f L_a(1 + \mathbf{n} \cdot \mathbf{p}_a)} \right]. \quad (2)$$

where L_a is the distance from this pulsar to earth, and $F_a^A(\mathbf{n})$ is the PTA antenna response defined as

$$F_a^A(\mathbf{n}) \equiv \frac{p_a^i p_a^j e_{ij}^A(\mathbf{n})}{2(1 + \mathbf{n} \cdot \mathbf{p}_a)}. \quad (3)$$

The timing residual is the time integral of the redshift:

$$r_a(t) = \int^t dt' z_a(t'). \quad (4)$$

Hence, in the frequency domain,

$$\begin{aligned} \tilde{r}_a(f) &= \frac{\tilde{z}_a(f)}{2\pi i f} \\ &= \sum_A \int d\mathbf{n} \frac{F_a^A(\mathbf{n})}{2\pi i f} h_A(f, \mathbf{n}) \left[1 - e^{2\pi i f L_a(1 + \mathbf{n} \cdot \mathbf{p}_a)} \right]. \end{aligned} \quad (5)$$

2.1. Isotropic background and HD ORF

Consider two pulsars with residual $\tilde{r}_a(f)$ and $\tilde{r}_b(f)$. For an isotropic, stationary, unpolarized stochastic background with one-sided strain PSD $S_h(f)$, it gives

$$\langle h_A(f, \mathbf{n}) h_{A'}^*(f', \mathbf{n}') \rangle = \frac{1}{2} \delta_{AA'} \delta(f - f') \frac{\delta^2(\mathbf{n}, \mathbf{n}')}{4\pi} S_h(f). \quad (6)$$

Using (5) and (6), the cross-spectrum of the residuals is then

$$\langle \tilde{r}_a(f) \tilde{r}_b^*(f') \rangle = \frac{1}{2} \delta(f - f') \Gamma_{ab}(f) \frac{S_h(f)}{12\pi^2 f^2}, \quad (7)$$

where

$$\Gamma_{ab}(f) = \frac{1}{2} \sum_A \int \frac{d\mathbf{n}}{4\pi} F_a^A(\mathbf{n}) F_b^A(\mathbf{n}) \kappa_{ab}(f, \mathbf{n}), \quad (8)$$

defines the frequency-dependent ORF, and

$$\kappa_{ab}(f, \mathbf{n}) = \left[1 - e^{2\pi i f L_a(1 + \mathbf{n} \cdot \mathbf{p}_a)} \right] \left[1 - e^{-2\pi i f L_b(1 + \mathbf{n} \cdot \mathbf{p}_b)} \right]. \quad (9)$$

Under the approximation $2\pi f L \gg 1$, only the constant term (the EE term) survives: $\kappa_{ab}(f, \mathbf{n}) \rightarrow 1$, while the other terms oscillate rapidly and average to zero.

Using polarization-sum identity, the angular integration on the sphere yields the standard Hellings–Downs (HD) curve, with the convention $\Gamma_{aa} = 1$:

$$\Gamma_{ab}^{\text{HD}}(\zeta) = \frac{3}{2} \left[x \ln x - \frac{1}{6} x + \frac{1}{3} \right], \quad (10)$$

where $x \equiv \frac{1 - \cos \zeta}{2}$, and ζ is the separation angle between two pulsars a and b .

2.2. Anisotropic backgrounds and directional ORFs

If the gravitational wave background has an angular distribution $P(\mathbf{n})$, then

$$\langle h_A(f, \mathbf{n}) h_{A'}^*(f', \mathbf{n}') \rangle = \frac{1}{2} \delta_{AA'} \delta(f - f') \delta^2(\mathbf{n}, \mathbf{n}') S_h(f) P(\mathbf{n}), \quad (11)$$

where $P(\mathbf{n})$ is the angular distribution of GW power on the sky, and the ORF becomes

$$\Gamma_{ab}(f) = \frac{1}{2} \sum_A \int d\mathbf{n} F_a^A(\mathbf{n}) F_b^A(\mathbf{n}) \kappa_{ab}(f, \mathbf{n}) P(\mathbf{n}). \quad (12)$$

The angular distribution $P(\mathbf{n})$ could be further expanded with spherical-harmonics as $P(\mathbf{n}) = \sum_{\ell m} c_{\ell m} Y_{\ell m}(\mathbf{n})$. Take it back into 12 we have

$$\Gamma_{ab}(f) = \sum_{\ell m} c_{\ell m} \Gamma_{ab}^{\ell m}(f), \quad (13)$$

where

$$\Gamma_{ab}^{\ell m}(f) = \frac{1}{2} \sum_A \int d\mathbf{n} F_a^A(\mathbf{n}) F_b^A(\mathbf{n}) \kappa_{ab}(f, \mathbf{n}) Y_{\ell m}(\mathbf{n}). \quad (14)$$

In the short-wavelength approximation, only the Earth-Earth term survives the integration in Eq. 12, which writes

$$\Gamma_{ab} = \int d\mathbf{n} P(\mathbf{n}) \mathcal{F}_{ab}(\mathbf{n}),$$

$$\mathcal{F}_{ab}(\mathbf{n}) \equiv \frac{1}{2} \sum_{A=+, \times} F_a^A(\mathbf{n}) F_b^A(\mathbf{n}). \quad (15)$$

The isotropic case corresponds to the single $\ell = 0, m = 0$ mode, which has $P(\mathbf{n}) = 1/(4\pi)$ and one recovers the HD correlation pattern.

3. RELATING SGWB ANISOTROPY TO CLUSTERING OF LSS

Physically, the nanohertz SGWB is expected to be dominated by a finite population of astrophysical sources, most notably SMBHBs. Since SMBHBs typically reside in galactic nuclei and galaxies trace the distribution of dark matter halos (e.g., Ferrarese & Merritt 2000; Gebhardt et al. 2000; Kormendy & Ho 2013; Reines & Volonteri 2015; Matthee et al. 2025), SMBHBs are expected to follow the cosmic LSS to some degree. Motivated by this expectation, we introduce an LSS-informed angular modulation of the background, promoting $P(\mathbf{n})$ from a constant to an anisotropic field. A minimal and widely used phenomenological ansatz is that the GW anisotropy traces the galaxy overdensity in a redshift-dependent manner,

$$\delta_{\text{gw}}(\mathbf{n}, z) = c(z) \delta_{\text{gal}}(\mathbf{n}, z), \quad (16)$$

where $\delta_{\text{gal}}(\mathbf{n}, z)$ denotes the galaxy overdensity as a function of sky direction \mathbf{n} and redshift z (e.g., in tomographic redshift slices), and $c(z)$ encodes how strongly the SGWB anisotropy traces the galaxies as a function of z .

3.1. LSS-template ORF

To connect this to the ORF, we allow the angular weight to receive contributions from all redshifts along the line of sight,

$$P(\mathbf{n}) = \frac{1}{4\pi} \left[1 + \int_{z_{\min}}^{z_{\max}} dz \delta_{\text{gw}}(\mathbf{n}, z) \right]$$

$$= \frac{1}{4\pi} \left[1 + \int_{z_{\min}}^{z_{\max}} dz c(z) \delta_{\text{gal}}(\mathbf{n}, z) \right]. \quad (17)$$

Inserting (17) into (15) and using linearity yields a decomposition into an isotropic (HD-like) piece plus an LSS-weighted anisotropic contribution integrated over redshift:

$$\Gamma_{ab} = \int \frac{dn}{4\pi} \mathcal{F}_{ab}(\mathbf{n})$$

$$+ \frac{1}{4\pi} \int_{z_{\min}}^{z_{\max}} dz c(z) \int d\mathbf{n} \delta_{\text{gal}}(\mathbf{n}, z) \mathcal{F}_{ab}(\mathbf{n})$$

$$= \Gamma_{ab}^{\text{HD}} + \frac{1}{4\pi} \int_{z_{\min}}^{z_{\max}} dz c(z) \Gamma_{ab}^{\delta_{\text{gal}}}(z; \mathbf{p}_a, \mathbf{p}_b), \quad (18)$$

where

$$\Gamma_{ab}^{\delta_{\text{gal}}}(z; \mathbf{p}_a, \mathbf{p}_b) \equiv \int d\mathbf{n} \delta_{\text{gal}}(\mathbf{n}, z) \mathcal{F}_{ab}(\mathbf{n}) \quad (19)$$

is the correlation template obtained by weighting the PTA response kernel by the galaxy overdensity map. The first term in (18) gives the HD ORF term, and the second term gives the anisotropic ORF, i.e., the LSS ORF term tracing galaxy overdensity map.

Adopt the complex spherical-harmonic convention

$$\delta_{\text{gal}}(\mathbf{n}, z) \equiv \sum_{\ell=\ell_{\min}}^{\ell_{\max}} \sum_{m=-\ell}^{\ell} a_{\ell m}(z) Y_{\ell m}(\mathbf{n}), \quad (20)$$

where

$$a_{\ell m}(z) = \int d\mathbf{n} \delta_{\text{gal}}(\mathbf{n}, z) Y_{\ell m}^*(\mathbf{n}). \quad (21)$$

Define the spherical-harmonic response basis matrices

$$G_{\ell m}^{ab} \equiv \int d\mathbf{n} Y_{\ell m}(\mathbf{n}) \mathcal{F}_{ab}(\mathbf{n}). \quad (22)$$

Then, we have

$$\Gamma_{ab}^{\delta_{\text{gal}}} = \sum a_{\ell m} G_{\ell m}^{ab}. \quad (23)$$

3.2. LSS ORF setting for inference

In practice, we discretize the redshift range into N bins, $[z_{\min}, z_{\max}] = \bigcup_{i=1}^N [z_i, z_{i+1}]$, and approximate $c(z)/(4\pi)$ as piecewise constant within each bin,

$$\frac{c(z)}{4\pi} \equiv \epsilon(z) \simeq \epsilon_i, \quad \text{for } z \in [z_i, z_{i+1}]. \quad (24)$$

We then define the binned LSS ORF template as the redshift-integrated contribution in the i th bin,

$$\Gamma_{ab}^{\text{LSS}(i)} \equiv \int_{z_i}^{z_{i+1}} dz \Gamma_{ab}^{\delta_{\text{gal}}}(z; \mathbf{p}_a, \mathbf{p}_b), \quad (25)$$

so that Eq. (18) can be written as

$$\Gamma_{ab} \simeq \Gamma_{ab}^{\text{HD}} + \sum_{i=1}^N \epsilon_i \Gamma_{ab}^{\text{LSS}(i)}. \quad (26)$$

Using the HEALPix pixelization, we discretize the sky into $N_{\text{pix}} = 12 N_{\text{side}}^2$, where N_{side} is the HEALPix resolution parameter. In this work, we adopt $N_{\text{side}} = 64$. Eq. (22) is then evaluated numerically via a approximation over pixel centers,

$$G_{\ell m}^{ab} \simeq \Delta\Omega \sum_{i=1}^{N_{\text{pix}}} Y_{\ell m}(\Omega_i) \mathcal{F}_{ab}(\Omega_i), \quad (27)$$

where $\Delta\Omega \equiv 4\pi/N_{\text{pix}}$, and Ω_i denotes the direction of the i th pixel center and $\Delta\Omega$ is the solid angle per pixel. Furthermore, finite pixelization can introduce small imaginary components and mild asymmetry; we therefore project the numerically evaluated ORF onto the real, symmetric subspace,

$$\Gamma^{\text{LSS}} \leftarrow \Re(\Gamma^{\text{LSS}}), \quad \Gamma^{\text{LSS}} \leftarrow \frac{1}{2} (\Gamma^{\text{LSS}} + (\Gamma^{\text{LSS}})^{\text{T}}). \quad (28)$$

4. CONSTRUCTION OF LOW- ℓ LSS SPHERICAL-HARMONIC COEFFICIENTS

In this section we construct low-multipole spherical-harmonic coefficients $a_{\ell m}$ of the LSS galaxy overdensity field for certain redshift slices. Our goal is to obtain a set of stable, cut-sky-robust coefficients up to ℓ_{max} that can be used as input templates in the PTA low- ℓ LSS ORF analysis.

4.1. 2MPZ galaxy sample and redshift slicing

We use the *2MASS Photometric Redshift* catalogue (2MPZ, Bilicki et al. (2014)) to trace the angular distribution of nearby galaxies and construct redshift-sliced LSS templates for our PTA analysis. 2MPZ contains $\sim 10^6$ galaxies over (nearly) the full sky and provides homogeneous photometric redshifts ($\sigma_z \simeq 0.015$) from cross-matching 2MASS XSC with WISE and SuperCOSMOS (Bilicki et al. 2014). The catalog primarily probes the low-redshift Universe (with most objects at $z \lesssim 0.3$), making it straightforward to build tomographic templates in the slices $0 < z \leq 0.1$ and $0.1 < z \leq 0.2$; the bin width $\Delta z = 0.1$ is substantially larger than the

typical photometric-redshift scatter, which helps mitigate inter-bin leakage. These features make 2MPZ well suited for PTA applications: its wide sky coverage helps mitigate cut-sky mode coupling for the largest angular modes, its near-/mid-IR selection mitigates sensitivity to Galactic extinction compared to optical-only samples, and its low-redshift depth provides a natural tracer for constructing LSS templates relevant to low- ℓ ORF analyses.

We divide the catalogue into two photometric-redshift bins, **bin 1** : $0 < z < 0.1$ and **bin 2** : $0.1 < z < 0.2$, and treat each slice as an independent LSS anisotropy template. From each slice we build overdensity maps on a common pixelization and estimate stable low- ℓ spherical-harmonic coefficients $\{a_{\ell m}\}$ up to ℓ_{max} on the masked sky. These coefficients are then used to construct the corresponding PTA LSS-ORF templates, $\Gamma_{ij}^{\text{LSS}}(\mathbf{bin1})$ and $\Gamma_{ij}^{\text{LSS}}(\mathbf{bin2})$, which enter the mixed-ORF models analyzed in the following sections.

4.2. Galaxy counts and overdensity map in equatorial coordinates

For each redshift bin we start from a galaxy catalog containing right ascension and declination (α, δ) . We pixelize the catalog into a HEALPix map at resolution N_{side} by counting galaxies per pixel,

$$N(p) \equiv \sum_{g \in \text{catalog}} \mathbf{1}[g \in p], \quad (29)$$

where p labels HEALPix pixels and $\mathbf{1}$ is the indicator function. Throughout, we work in the equatorial (celestial) coordinate system, i.e. we identify the spherical angles as $\theta = \pi/2 - \delta$ and $\phi = \alpha$.

We impose a Galactic-plane cut by defining a binary sky mask based on Galactic latitude $b(\mathbf{n})$:

$$M_{\text{bin}}(\mathbf{n}) = \begin{cases} 1, & |b(\mathbf{n})| \geq b_{\text{cut}}, \\ 0, & \text{otherwise,} \end{cases} \quad (30)$$

where $b_{\text{cut}} = 20^\circ$ in our fiducial setup, and \mathbf{n} is the unit vector specifying a sky direction associated with each equatorial HEALPix pixel. Although b is computed in Galactic coordinates, the mask is represented on the same equatorial HEALPix pixelization as the data map.

We define the mean number of galaxies per pixel using the binary mask,

$$\bar{N} \equiv \frac{\sum_p M_{\text{bin}}(p) N(p)}{\sum_p M_{\text{bin}}(p)}, \quad (31)$$

and construct the overdensity field

$$\delta(p) = \begin{cases} \frac{N(p) - \bar{N}}{\bar{N}}, & M_{\text{bin}}(p) = 1, \\ 0, & M_{\text{bin}}(p) = 0. \end{cases} \quad (32)$$

For subsequent power-spectrum estimation we further apodize the binary mask using a C^1 (C1) apodization kernel with scale θ_{apod} ,

$$M_{\text{apod}}(\mathbf{n}) \equiv \text{Apodize}[M_{\text{bin}}(\mathbf{n}); \theta_{\text{apod}}, \text{C1}], \quad (33)$$

with $\theta_{\text{apod}} = 2^\circ$ in the fiducial setup. The apodized mask is then used as the weight map in the MASTER (pseudo- C_ℓ) estimation, and is applied consistently in the spherical-harmonic analysis when reconstructing the (masked) harmonic coefficients.

4.2.1. Low- ℓ cleaning: weighted removal of monopole and dipole

To mitigate contamination from large-scale offsets and dipolar systematics, and their mode coupling under incomplete sky coverage, we optionally remove the monopole and dipole components of the overdensity field using a weighted least-squares fit on the apodized-mask support. Such monopole/dipole subtraction is commonly adopted in cut-sky pseudo- C_ℓ (MASTER) and correlation-function estimators, where the sky mask couples multipoles and can leak residual large-scale power into higher- ℓ modes (e.g., Hivon et al. 2002; Szapudi et al. 2001; Vielva et al. 2006; Alonso et al. 2019).

Let $\mathcal{P} = \{p : M_{\text{apod}}(p) > \tau\}$ be the set of unmasked pixels after thresholding with τ . In the fiducial setup we take $\tau = 10^{-3}$ to exclude extremely low-weight edge pixels introduced by apodization and improve numerical stability. We fit and subtract the $\ell \leq 1$ subspace,

$$\delta_{\text{used}}(p) \equiv \delta(p) - \sum_{k=1}^4 \beta_k B_k(p), \quad p \in \mathcal{P}, \quad (34)$$

where $\{B_k\}$ are real-valued basis maps spanning the $\ell \leq 1$ subspace (e.g., Y_{00} , Y_{10} , and the Re/Im components of Y_{11}) evaluated on the HEALPix grid, and the coefficients β_k minimize

$$\boldsymbol{\beta} = \arg \min_{\boldsymbol{\beta}} \sum_{p \in \mathcal{P}} M_{\text{apod}}(p) \left[\delta(p) - \sum_{k=1}^4 \beta_k B_k(p) \right]^2. \quad (35)$$

Pixels outside \mathcal{P} are set to zero in δ_{used} .

4.3. MAP reconstruction of $a_{\ell m}$ on the cut sky

We reconstruct the low- ℓ harmonic coefficients by fitting a truncated spherical-harmonic expansion to the cut-sky field,

$$\delta_{\text{used}}(\hat{\mathbf{n}}) \approx \sum_{\ell=2}^{\ell_{\text{max}}} \sum_{m=-\ell}^{\ell} a_{\ell m} Y_{\ell m}(\hat{\mathbf{n}}), \quad (36)$$

following the standard Wiener/MAP reconstruction framework for Gaussian random fields with incomplete sky coverage (e.g., Lahav et al. 1994; Zaroubi

et al. 1995). Restricting to pixels $p \in \mathcal{P}$, we form the data vector $y_p \equiv \delta_{\text{used}}(p)$ and adopt pixel weights $w_p \equiv M_{\text{apod}}(p)$. To work entirely in real arithmetic, we parameterize the unknown coefficients as

$$\boldsymbol{\theta} \equiv \left(\{a_{\ell 0}\}, \{\text{Re } a_{\ell m}\}_{m>0}, \{\text{Im } a_{\ell m}\}_{m>0} \right), \quad (37)$$

and write the linear model $\mathbf{y} \approx \mathbf{X}\boldsymbol{\theta}$, where the design matrix \mathbf{X} is constructed by evaluating the corresponding real-valued basis maps on the HEALPix grid.

Assuming Gaussian pixel noise with diagonal weight matrix $\mathbf{W} = \text{diag}(w_p)$, the negative log-likelihood is

$$-2 \ln \mathcal{L}(\boldsymbol{\theta}) = (\mathbf{y} - \mathbf{X}\boldsymbol{\theta})^\top \mathbf{W} (\mathbf{y} - \mathbf{X}\boldsymbol{\theta}). \quad (38)$$

We further impose a Gaussian prior on the low- ℓ harmonic coefficients, with a diagonal prior precision given by the inverse signal covariance as in standard Wiener-filter/MAP reconstructions (e.g., Lahav et al. 1994; Zaroubi et al. 1995; Bunn et al. 1994). In particular, we adopt a data-driven prior covariance by setting its angular power spectrum to the target spectrum C_ℓ^{target} , estimated from the masked map via MASTER bandpowers computed with NaMaster (Hivon et al. 2002; Alonso et al. 2019); see subsection 4.3.1. For a real field this corresponds to $\text{Var}(a_{\ell 0}) = C_\ell^{\text{target}}$ and $\text{Var}(\text{Re } a_{\ell m}) = \text{Var}(\text{Im } a_{\ell m}) = C_\ell^{\text{target}}/2$ for $m > 0$. Equivalently,

$$-2 \ln \pi(\boldsymbol{\theta}) = \boldsymbol{\theta}^\top \boldsymbol{\Lambda} \boldsymbol{\theta}, \quad \Lambda_{kk} = \begin{cases} 1/C_\ell^{\text{target}}, & a_{\ell 0}, \\ 2/C_\ell^{\text{target}}, & \text{Re/Im } a_{\ell m} \ (m > 0). \end{cases} \quad (39)$$

where each diagonal element is associated with the appropriate (ℓ, m) component.

The MAP estimate $\boldsymbol{\theta}$ via finding the minimal of $(\mathbf{y} - \mathbf{X}\boldsymbol{\theta})^\top \mathbf{W} (\mathbf{y} - \mathbf{X}\boldsymbol{\theta}) + \lambda \boldsymbol{\theta}^\top \boldsymbol{\Lambda} \boldsymbol{\theta}$, where λ is a tunable regularization strength, scaled in practice to yield numerically stable conditioning. We adopt $\lambda = 1$ for the fiducial analysis (see Appendix A.2 for the details). Then the solution writes

$$(\mathbf{X}^\top \mathbf{W} \mathbf{X} + \lambda \boldsymbol{\Lambda}) \boldsymbol{\theta} = \mathbf{X}^\top \mathbf{W} \mathbf{y}. \quad (40)$$

The mapping from $\boldsymbol{\theta}$ back to the complex coefficients $a_{\ell m}$ for $m \geq 0$ is straightforward, and the coefficients for negative m follow from the reality condition

$$a_{\ell, -m} = (-1)^m a_{\ell m}^*. \quad (41)$$

4.3.1. Target spectrum from NaMaster

We estimate the target angular power spectrum using the MASTER (pseudo- C_ℓ) approach implemented

in NaMaster (Hivon et al. 2002; Alonso et al. 2019). We define a masked (apodized) field

$$f(\mathbf{n}) \equiv M_{\text{apod}}(\mathbf{n}) \delta_{\text{used}}(\mathbf{n}), \quad (42)$$

and compute the coupled pseudo-spectrum \tilde{C}_ℓ from f . In the MASTER formalism, the sky mask couples multipoles such that, in expectation,

$$\langle \tilde{C}_\ell \rangle = \sum_{\ell'} \mathbf{M}_{\ell\ell'} C_{\ell'} + \tilde{N}_\ell, \quad (43)$$

where \mathbf{M} is the mode-coupling matrix determined by the mask, and \tilde{N}_ℓ includes the shot-noise contribution.

We perform a binned (bandpower) deconvolution with linear bins of width $\Delta\ell \equiv n_{\ell b}$, obtaining deconvolved bandpowers C_b^{MASTER} and their effective multipoles ℓ_{eff} . Optionally, we subtract a Poisson shot-noise bias for the number-count overdensity field, approximated as a white spectrum,

$$C_{\text{shot}} \simeq \frac{1}{\bar{n}}, \quad \bar{n} \equiv \frac{N_{\text{gal}}^{(\text{mask})}}{4\pi f_{\text{sky}}}, \quad f_{\text{sky}} \equiv \frac{1}{4\pi} \int d\mathbf{n} M_{\text{bin}}(\mathbf{n}), \quad (44)$$

where $N_{\text{gal}}^{(\text{mask})}$ is the number of galaxies within the binary mask M_{bin} . Since the spectrum is used only as a positive-definite target prior, we set $C_b^{\text{MASTER}} \leftarrow \max(C_b^{\text{MASTER}} - C_{\text{shot}}, 0)$.

For use as a prior in the harmonic reconstruction we interpolate the binned spectrum onto the integer multipole grid,

$$C_\ell^{\text{target}} \equiv \text{interp}(\ell; \{\ell_{\text{eff}}\}, \{C_b^{\text{MASTER}}\}), \quad (45)$$

and enforce a small positive floor to avoid numerical issues at very low power.

4.3.2. Per-multipole rescaling

The MAP solution in Eq. (40) yields a set of spherical-harmonic coefficients $a_{\ell m}^{\text{MAP}}$ that are numerically stable on the cut sky. However, the corresponding full-sky spectrum,

$$C_\ell^{\text{MAP}} \equiv \frac{1}{2\ell + 1} \sum_{m=-\ell}^{\ell} |a_{\ell m}^{\text{MAP}}|^2, \quad (46)$$

does not, in general, coincide exactly with the adopted target spectrum C_ℓ^{target} . To enforce consistency at the bandpower level, we apply an isotropic, per-multipole rescaling, to the final coefficients $a_{\ell m}$:

$$a_{\ell m} = s_\ell a_{\ell m}^{\text{MAP}}, \quad s_\ell \equiv \left(\frac{C_\ell^{\text{target}}}{C_\ell^{\text{MAP}}} \right)^{1/2}, \quad (47)$$

which guarantees the final spectrum $C_\ell = C_\ell^{\text{target}}$ by construction while preserving the relative phases among

the m -modes at fixed ℓ . The final coefficients $\{a_{\ell m}\}$ for $\ell \in [2, \ell_{\text{max}}]$ are then stored (for both redshift bins) and used to build the corresponding low- ℓ LSS ORF templates in the PTA analysis.

4.4. Low- ℓ reconstruction of LSS spherical-harmonic maps

The present analysis utilizes the 15-year NANOGrav timing data for 67 pulsars, determined by observational availability and data quality. Due to the finite and sparse sky coverage of the current array, it is primarily sensitive to the largest angular scales of the SGWB.

For this PTA configuration, the ORFs act as a strong low-pass filter in harmonic space, efficiently suppressing contributions from higher-order multipoles. Consequently, we truncate the LSS harmonic expansion at $\ell_{\text{max}} = 12$, which ensures convergence of the ORF Γ_{ab}^{LSS} and is consistent with existing anisotropy studies that primarily constrain only the lowest-order multipoles (Agazie et al. 2023; Hotinli et al. 2019; Taylor & Gair 2013). Sensitivity to higher- ℓ modes is expected to improve with future datasets featuring a larger number of well-distributed pulsars.

To assess whether the recovered low- ℓ structure is dominated by counting noise, we compare C_ℓ reconstructed following the method framed in sections 4.1–4.3 to the overdensity shot-noise level, which writes

$$\left[\frac{C_\ell}{C_{\text{shot}}} \right]_{\ell \in [2, 12]}. \quad (48)$$

The clustering power at $\ell \in [2, 12]$ exceeds the Poisson level by large factors with $C_\ell/C_{\text{shot}} \sim \mathcal{O}(10^2)$ for $z < 0.1$ and $\sim \mathcal{O}(10^1\text{--}10^2)$ for $0.1 < z < 0.2$, implying that the recovered low- ℓ modes are not dominated by counting noise.

Furthermore, for our fiducial mask choice ($b_{\text{min}} = 20^\circ$, apodization 2°), the off-diagonal correlation of the recovered coefficients remains moderate with $\max_{i \neq j} |\text{Corr}(a_i, a_j)| \sim 0.3$ for $\ell \in [2, 12]$ (see A.1 for the definition), indicating that mode coupling from the cut sky does not lead to catastrophic degeneracies at the multipoles used in this work. These diagnostics support the use of the reconstructed coefficients as a stable low-dimensional summary of the observed LSS for building the ORF templates used in this work.

Figure 1 displays the reconstructed LSS overdensity maps for two redshift bins from the 2MPZ catalog, following the method outlined in the preceding sections. These maps are derived by truncating the spherical-harmonic expansion of the galaxy overdensity field at $2 \leq \ell \leq 12$, retaining only the large-angular-scale modes. The black dashed lines delineate the regions

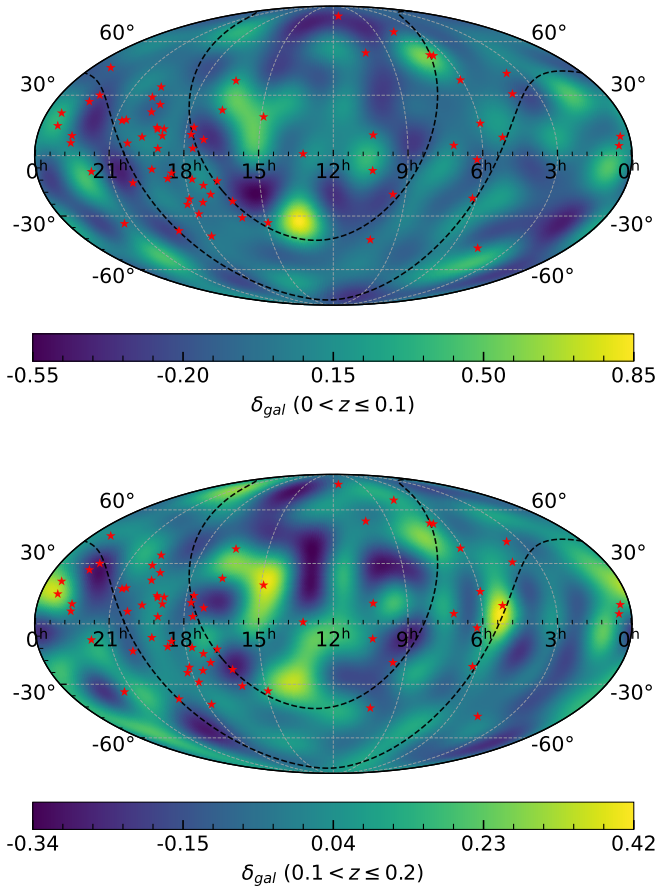


Figure 1. Reconstructed large-scale-structure overdensity maps from spherical-harmonic coefficients $a_{\ell m}$ inferred from the 2MPZ galaxy catalog, truncated to $2 \leq \ell \leq 12$, for the two redshift bins used in this work. The maps are shown in a Mollweide projection in equatorial coordinates. Red stars mark the sky positions of the 67 pulsars in our PTA sample. The black dashed curves delineate the mask boundary around the Galactic plane, defined using a Galactic latitude cut.

corresponding to the Galactic plane mask (Eq. (30)), applied to mitigate stellar contamination and extinction effects.

Within the unmasked sky, the reconstructed maps capture the low-order angular features of the large-scale distribution of nearby galaxies. Differences between the two redshift bins arise from the evolution of LSS and cosmic variance, though similar structures are observed across both maps. These low- ℓ maps form the basis for constructing the low-redshift LSS-induced anisotropic ORFs used in the PTA analysis.

5. CONSTRAINTS ON LSS-MODULATED ORFS

We now present the results of Bayesian inference on PTA data using phenomenological ORF models that include a contribution correlated with the

observed LSS. Following the NANOGrav 15-year stochastic analysis setup (Agazie et al. 2023a), we fix the white-noise parameters to the released backend-dependent values in the 15yr noise dictionary, and analytically marginalize timing-model uncertainties using `MarginalizingTimingModel` with `use_svd=True`. We represent red processes in a Fourier basis with $f_k = k/T_{\text{span}}$, where $T_{\text{span}} = \max(t_{\text{max}}) - \min(t_{\text{min}})$ is the array timespan; we use 30 frequency components for intrinsic pulsar red noise and $N_f = 14$ components for the common SGWB term (and hence for ORF-modulated correlations), matching the NANOGrav 15-year GWB search configuration. In all cases, the baseline isotropic model corresponds to the HD ORF, while anisotropy is introduced through one or more fixed-shape LSS templates constructed from the 2MPZ galaxy catalogue in the low-redshift slices described in Section 4, with each LSS-correlated contribution controlled by a dimensionless mixing coefficient ϵ (and $\epsilon = 0$ reducing to the pure-HD hypothesis).

5.1. Single-bin LSS-correlated ORF

We first consider models in which the isotropic HD correlation is augmented by a single LSS template constructed from one redshift slice,

$$\Gamma_{ab} = \Gamma_{ab}^{\text{HD}} + \epsilon_i \Gamma_{ab}^{\text{LSS}(i)}, \quad (49)$$

where $i = 1, 2$ labels the redshift bins, $\Gamma_{ab}^{\text{LSS}(i)}$ is the corresponding LSS-derived ORF template (Section 4), and ϵ_i parametrizes the relative amplitude of the LSS-correlated anisotropic component in that bin. Positive (negative) ϵ_i corresponds to a component correlated (anti-correlated) with the LSS template.

Figure 2 illustrates how an LSS-correlated contribution modifies the HD correlation at the level of individual pulsar pairs. For an isotropic background, Γ_{ab} is uniquely determined by the separation ζ_{ab} , producing a single curve. Adding the anisotropic template Γ^{LSS} breaks this one-to-one mapping: pairs with the same ζ_{ab} can have different Γ_{ab} depending on their sky locations relative to the fixed LSS pattern. This leads to a characteristic spread of pairwise ORF values around the HD curve, with a magnitude that increases with $|\epsilon|$ (compare $\epsilon = 1$ to $\epsilon = 3$). The detailed distribution of points differs between the two redshift slices because the underlying LSS maps are not identical, leading to different projections onto the sparse PTA sky sampling.

The posterior distributions for the single-bin mixed-ORF models are shown in Figures 3 and 4. In both redshift slices, the inferred mixing amplitude is consistent with $\epsilon_i = 0$, with $\epsilon_1 = 0.20^{+1.68}_{-1.66}$ and $\epsilon_2 = -0.11^{+2.04}_{-1.83}$ (median and 68% credible intervals). The breadth of

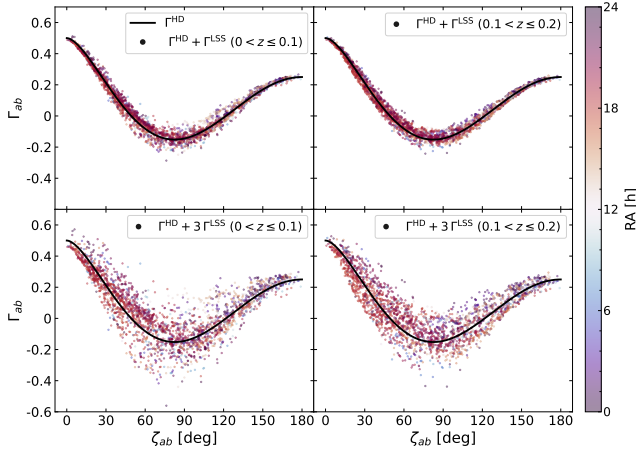


Figure 2. Pairwise ORF values Γ_{ab} versus pulsar angular separation ζ_{ab} for the model $\Gamma_{ab} = \Gamma_{ab}^{\text{HD}} + \epsilon \Gamma_{ab}^{\text{LSS}}$. The solid black curve shows the HD prediction. Colored points show Γ_{ab} evaluated for individual pulsar pairs and are colored by the pair-midpoint right ascension (RA, in hours). Left/right columns correspond to the 2MPZ redshift slices $0 < z \leq 0.1$ and $0.1 < z \leq 0.2$, respectively; top/bottom rows adopt $\epsilon = 1$ and $\epsilon = 3$.

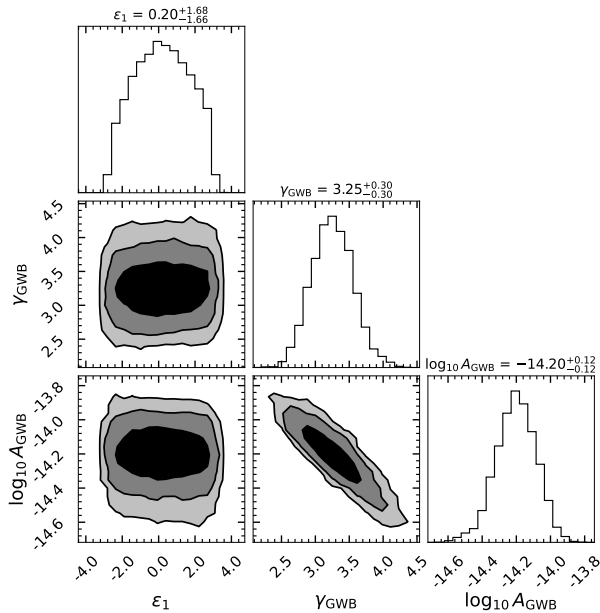


Figure 3. Marginalized posterior distribution for $(\epsilon_1, \gamma_{\text{gw}}, \log_{10} A_{\text{gw}})$ in the single-bin model $\Gamma = \Gamma^{\text{HD}} + \epsilon_1 \Gamma^{\text{LSS}(1)}$, where $\Gamma^{\text{LSS}(1)}$ is derived from the 2MPZ slice $0 < z \leq 0.1$. Diagonal panels show 1D marginalized posteriors and off-diagonal panels show joint credible regions. Titles report the median and 68% credible intervals.

these posteriors implies that, within the sensitivity of the present dataset, the analysis primarily yields upper limits on the amplitude of any 2MPZ-template-correlated contribution, rather than a statistically sig-

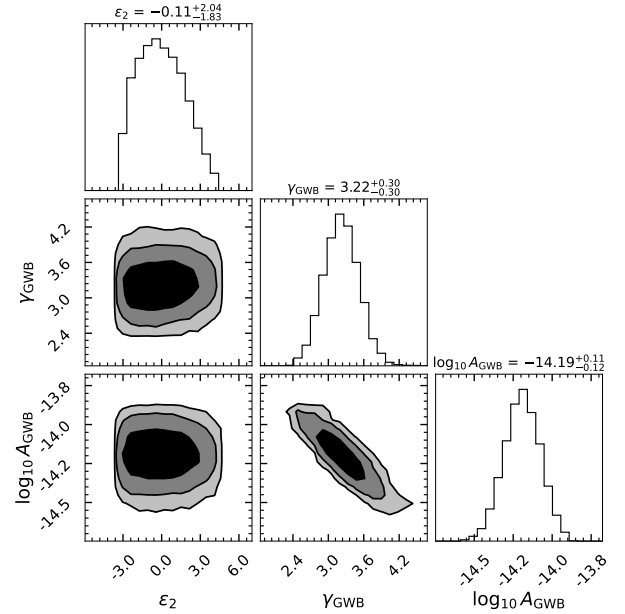


Figure 4. Same as Figure 3, but for $(\epsilon_2, \gamma_{\text{gw}}, \log_{10} A_{\text{gw}})$ in the model $\Gamma = \Gamma^{\text{HD}} + \epsilon_2 \Gamma^{\text{LSS}(2)}$, where $\Gamma^{\text{LSS}(2)}$ is derived from the 2MPZ slice $0.1 < z \leq 0.2$.

nificant detection of correlated structure. Any detailed, pair-by-pair substructure in the LSS-correlated ORF presented in Figure 2 is therefore either absent or not yet statistically resolvable with the current 15-year dataset. Meanwhile, the GWB spectral parameters $\log_{10} A_{\text{GWB}}$ and γ_{GWB} retain their usual power-law degeneracy, and their joint posterior shows no pronounced correlation with ϵ_i , indicating that allowing an LSS-modulated degree of freedom does not materially shift the inferred isotropic-background parameters.

5.2. Two-bin LSS-correlated ORF

We next consider a more general phenomenological ORF model that allows independent LSS-correlated contributions from both 2MPZ redshift slices,

$$\Gamma_{ab} = \Gamma_{ab}^{\text{HD}} + \epsilon_1 \Gamma_{ab}^{\text{LSS}(1)} + \epsilon_2 \Gamma_{ab}^{\text{LSS}(2)}, \quad (50)$$

where ϵ_1 and ϵ_2 parameterize the amplitudes of the two fixed-shape LSS-modulated templates constructed from the low-redshift 2MPZ slices.

The marginalized posterior for the two-bin model is shown in Figure 5. Both anisotropy parameters remain consistent with zero, $\epsilon_1 = 0.37^{+1.80}_{-1.91}$ and $\epsilon_2 = -0.20^{+2.26}_{-2.14}$ (median and 68% credible intervals), while the inferred $(\log_{10} A_{\text{gw}}, \gamma_{\text{gw}})$ are consistent with the single-bin analyses. A prominent feature of the joint posterior is an elongated, tilted support in the (ϵ_1, ϵ_2) plane, indicating a strong degeneracy between the two coefficients. This behavior reflects the fact that the current 15-year PTA

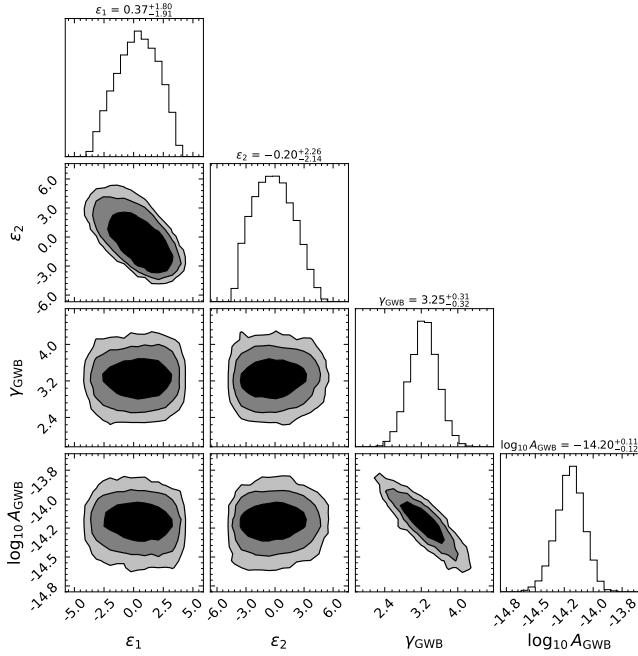


Figure 5. Marginalized posterior distribution for $(\epsilon_1, \epsilon_2, \gamma_{\text{GWB}}, \log_{10} A_{\text{GWB}})$ in the two-bin model $\Gamma = \Gamma^{\text{HD}} + \epsilon_1 \Gamma^{\text{LSS}(1)} + \epsilon_2 \Gamma^{\text{LSS}(2)}$. The joint posterior exhibits a strong degeneracy between ϵ_1 and ϵ_2 , consistent with partial non-orthogonality of the two LSS templates under the PTA sampling of pulsar pairs. Titles report the median and 68% credible intervals.

dataset does not cleanly disentangle two non-orthogonal, fixed-shape low-redshift LSS templates when projected onto the finite set of pulsar pairs; instead, it primarily constrains particular linear combinations of (ϵ_1, ϵ_2) .

To quantify and visualize this degeneracy, we compute the Pearson correlation coefficient

$$\rho(\epsilon_1, \epsilon_2) \equiv \frac{\text{Cov}(\epsilon_1, \epsilon_2)}{\sqrt{\text{Var}(\epsilon_1) \text{Var}(\epsilon_2)}}, \quad (51)$$

which is $\rho(\epsilon_1, \epsilon_2) = -0.61$ for this run, indicating a substantial anti-correlation. We further rotate (ϵ_1, ϵ_2) into the principal-component basis of their posterior covariance matrix. Concretely, letting \mathbf{C} denote the 2×2 covariance of (ϵ_1, ϵ_2) , we diagonalize \mathbf{C} and use its orthonormal eigenvectors to define new coordinates

$$\begin{pmatrix} \epsilon_{\parallel} \\ \epsilon_{\perp} \end{pmatrix} = \mathbf{U}^T \begin{pmatrix} \epsilon_1 \\ \epsilon_2 \end{pmatrix}, \quad (52)$$

where \mathbf{U} is the orthonormal matrix whose columns are the eigenvectors of \mathbf{C} . By construction, ϵ_{\parallel} corresponds to the eigen-direction with the smaller eigenvalue and is therefore the tightly constrained combination, whereas ϵ_{\perp} corresponds to the larger-eigenvalue direction and is the more weakly constrained orthogonal combination.

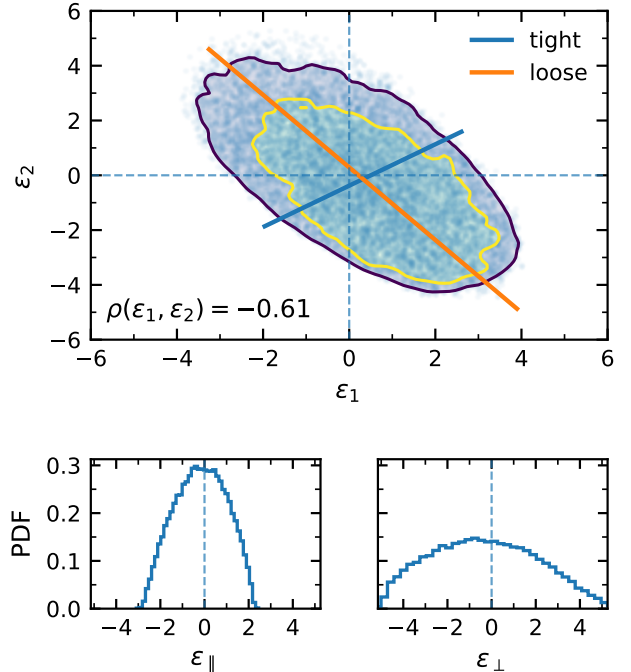


Figure 6. PCA visualization of the (ϵ_1, ϵ_2) degeneracy in the two-bin model. *Top*: joint posterior in the (ϵ_1, ϵ_2) plane with 68% and 95% credible contours, overlaid with the principal axes of the posterior covariance (“tight” and “loose”). The annotation reports the Pearson correlation coefficient $\rho(\epsilon_1, \epsilon_2)$ (Eq. (51)). *Bottom*: marginalized posteriors of the projected combinations ϵ_{\parallel} (tightly constrained principal component) and ϵ_{\perp} (more weakly constrained orthogonal component), illustrating that the data predominantly constrain one linear combination of the two LSS template amplitudes.

Figure 6 summarizes the Principal Component Analysis (PCA) interpretation: the 68% and 95% credible regions in the (ϵ_1, ϵ_2) plane are elongated along the principal axes, and the 1D posteriors of ϵ_{\parallel} and ϵ_{\perp} highlight the well- and poorly-constrained combinations, respectively.

5.3. Bayesian model comparison

We evaluate the relative support of the NANOGrav 15-year dataset for an LSS-modulated common-spectrum process, compared to the standard isotropic HD hypothesis, using hypermodel sampling. In this framework, a discrete model indicator is sampled jointly with the continuous timing-noise and GW parameters, enabling a direct inference of the evidence ratios between competing hypotheses.

For the single-bin LSS-correlated ORFs discussed in section 5.1, we obtain

$$\mathcal{B}_{\text{HD}+\text{LSS}_1, \text{HD}} = 0.40, \quad \mathcal{B}_{\text{HD}+\text{LSS}_2, \text{HD}} = 0.43, \quad (53)$$

both below unity. These values indicate that the current data do not provide evidence for an additional LSS-modulated degree of freedom beyond the isotropic HD correlations. Accordingly, the single-bin analyses constrain the amplitude of any SGWB component whose angular structure follows the low-redshift galaxy distribution traced by 2MPZ, while remaining consistent with statistical isotropy.

Finally, when allowing for a combined low-redshift LSS contribution, as has been discussed in section 5.2, we find

$$\mathcal{B}_{\text{HD}+\text{LSS}_1+\text{LSS}_2, \text{HD}} = 0.11. \quad (54)$$

The further reduction in the Bayes factor reflects the increased model complexity associated with introducing two LSS-correlation amplitudes: with the present PTA sensitivity and sky sampling, the data do not warrant the additional freedom, and the simpler isotropic HD model is preferred.

6. DISCUSSION AND CONCLUSION

In this work, we present the first Bayesian PTA likelihood analysis that embeds an externally observed, full-sky galaxy-survey LSS template directly as an ORF component. In our template-based framework, the pulsar-pair cross-correlations are modeled as a linear mixture of the isotropic Hellings–Downs (HD) form and one or more fixed, tomographic LSS-correlated templates,

$$\Gamma_{ab} = \Gamma_{ab}^{\text{HD}} + \sum_i \epsilon_i \Gamma_{ab}^{\text{LSS}(i)}, \quad (55)$$

where $\Gamma_{ab}^{\text{LSS}(i)}$ is constructed from the 2MPZ galaxy catalog (Bilicki et al. 2014) in redshift bin i . For a chosen normalization of $\Gamma_{ab}^{\text{LSS}(i)}$, the coefficient ϵ_i quantifies the relative admixture of an SGWB component whose pairwise angular correlations project onto that fixed LSS template, while the common-spectrum GW amplitude is fitted simultaneously with timing-noise parameters.

Applying this framework to the NANOGrav 15-year dataset (Agazie et al. 2023a,b), we find no statistically significant evidence for an LSS-correlated SGWB component traced by the 2MPZ templates. The posteriors are consistent with $\epsilon_i = 0$ in both single-bin and two-bin analyses (Figures 3–5), and the hypermodel Bayes factors are all below unity ($\mathcal{B}_{\text{HD}+\text{LSS}_1, \text{HD}} = 0.40$, $\mathcal{B}_{\text{HD}+\text{LSS}_2, \text{HD}} = 0.43$, $\mathcal{B}_{\text{HD}+\text{LSS}_{1+2}, \text{HD}} = 0.11$), indicating that the present data do not justify introducing additional LSS-correlated degrees of freedom beyond the HD hypothesis. This outcome is broadly consistent with existing PTA anisotropy searches, which mainly constrain departures from isotropy in the lowest-order multipoles beyond the monopole and currently report upper limits

rather than detections of anisotropy (e.g., Taylor et al. 2015; Agazie et al. 2023; Grunthal et al. 2024; Chen et al. 2026).

A key interpretational point is that our inference constrains template-correlated anisotropy rather than anisotropy in general. By construction, ϵ_i measures only the component of the SGWB whose pairwise correlations align with a specific, fixed low- z LSS template; it is therefore not a generic measure of the total anisotropic power on the sky. This distinction is particularly relevant for astrophysical SMBHB scenarios, where the nanohertz SGWB can be dominated by a finite number of contributing binaries. Poisson fluctuations in source counts and sky locations can then generate a realization-dependent “shot-noise” anisotropy component that is only weakly correlated with any particular low- ℓ galaxy template (e.g., Ravi et al. 2012; Cornish & Sesana 2013; Allen et al. 2024; Taylor et al. 2020; Bécsy et al. 2022; Konstandin et al. 2025). In practice, such a component acts as additional angular structure that increases variance, broadens the posterior on ϵ_i , and can suppress evidence for LSS modulation even if the ensemble-averaged SGWB is astrophysical and traces the matter distribution in a statistical sense.

Within these limitations, the present PTA data mainly provide upper limits on the amplitude of any 2MPZ-template-correlated contribution. Any detailed, pair-by-pair substructure in the ORF associated with such an LSS-correlated component (Figure 2) is therefore either absent or not yet statistically resolvable with the current 15-year dataset. In the single-bin analyses, the posteriors remain consistent with $\epsilon_i = 0$, yielding $\epsilon_1 = 0.20_{-1.66}^{+1.68}$ and $\epsilon_2 = -0.11_{-1.83}^{+2.04}$ (Figures 3–4). This indicates that the current dataset does not yet provide statistically significant evidence for an LSS-correlated component traced by these low-redshift templates, and that improved sensitivity—e.g., higher-SNR PTA data with denser and more uniform sky coverage—will be required to discriminate such correlated structure.

Allowing two tomographic templates introduces a strong degeneracy between (ϵ_1, ϵ_2) , with $\rho(\epsilon_1, \epsilon_2) = -0.61$ (Figure 5). This behavior is expected: the two low- z templates are partially non-orthogonal in the low multipoles to which PTAs are most sensitive, and sparse/non-uniform pulsar sky sampling further reduces the effective dimensionality of the response. The PCA rotation (Figure 6) indicates that only one linear combination is preferentially constrained, whereas the orthogonal combination remains largely prior-dominated. Consequently, increasing the number of redshift slices without additional information (e.g., improved PTA angular resolution, orthogonalized template bases, or

external priors) may primarily increase degeneracies rather than substantially tighten per-bin constraints.

On the LSS side, we constructed the low- ℓ ($2 \leq \ell \leq 12$) overdensity templates via a regularized MAP reconstruction on the cut sky, anchored to a pseudo- C_ℓ target spectrum estimated with NaMaster (Hivon et al. 2002; Alonso et al. 2019). For our fiducial masking and apodization choices, compact diagnostics support the stability of the modes used to build the ORF templates: the low- ℓ clustering power exceeds the galaxy-counting Poisson level by large factors (subsection 4.4), and mask-induced inter-mode coupling remains moderate (Appendix A). Nevertheless, template-based correlation tests can be diluted by large-scale survey systematics that perturb both the recovered phases and amplitudes of the low- ℓ modes. A natural extension is therefore to propagate LSS-template uncertainties into the PTA likelihood and, where possible, to construct the templates from deeper and better-calibrated wide-area surveys with improved control of systematics.

Overall, this work provides a first dedicated search for LSS-correlated anisotropy using real PTA data within a Bayesian ORF-template likelihood framework. Looking ahead, two developments are especially well-motivated by the limitations identified here: (i) sys-

tematic injection-and-recovery studies to forecast detectability and expected constraints on ϵ_i as a function of PTA sensitivity and pulsar sky coverage, and (ii) extension of the LSS-correlated ORF framework to higher redshifts using multiple wide-area galaxy surveys. These steps will turn the present analysis into a predictive program: not only constraining LSS-correlated anisotropy in current data, but also forecasting when and how future PTAs can detect (or tightly bound) an SGWB component that traces the cosmic web.

This work was supported by the National Natural Science Foundation of China (Grant No. 12405068). This work used publicly released NANOGrav 15-year data products (Agazie et al. 2023b; The NANOGrav Collaboration 2025); the analysis and interpretations are those of the author and do not necessarily reflect the views of the NANOGrav Collaboration. This work made use of the 2MASS Photometric Redshift (2MPZ) galaxy catalog (Bilicki et al. 2014) and open-source Python packages, including `enterprise` (Ellis et al. 2020), `PTMCMCSampler` (Ellis & van Haasteren 2019), and `NaMaster` (Hivon et al. 2002; Alonso et al. 2019). Numerical calculations were performed on the HPC cluster of the National Supercomputing Center in Zhejiang.

APPENDIX

A. DIAGNOSTICS FOR THE LOW- ℓ RECONSTRUCTION

This appendix summarizes two compact diagnostics used in the main text to assess the stability of the low- ℓ ($\ell \leq 12$) reconstruction on a cut sky: (i) the maximum absolute off-diagonal correlation among the recovered coefficients, and (ii) the choice of the regularization strength λ adopted in the MAP reconstruction of the spherical-harmonic coefficients (Section 4.3).

A.1. Off-diagonal correlation of recovered coefficients

The likelihood and prior described in Eqs. 38 and 39 yields the coefficient covariance

$$\text{Cov}(\boldsymbol{\theta}) \approx (\mathbf{X}^T \mathbf{W} \mathbf{X} + \boldsymbol{\Lambda})^{-1}, \quad (\text{A1})$$

which propagates the measurement uncertainty to the recovered coefficients. Mode coupling induced by the cut sky and weighting can introduce correlations among the recovered coefficients. We quantify this through the correlation matrix

$$\text{Corr}(\theta_i, \theta_j) \equiv \frac{\text{Cov}_{ij}}{\sqrt{\text{Cov}_{ii} \text{Cov}_{jj}}}, \quad (\text{A2})$$

constructed from the covariance in Eq. (A1). As a compact scalar diagnostic of inter-mode coupling we report

$$\max_{i \neq j} |\text{Corr}(\theta_i, \theta_j)|, \text{ or equivalently, } \max_{i \neq j} |\text{Corr}(a_i, a_j)|, \quad (\text{A3})$$

i.e., the maximum absolute off-diagonal correlation among all distinct parameter pairs. Values $\ll 1$ indicate weak coupling between modes, while values approaching unity would signal near-degeneracies caused by mask-induced mixing.

A.2. Choice of the regularization strength λ

The parameter λ controls the bias–variance trade-off of the cut-sky inversion in Eq. (40). Since the reconstructed coefficients are ultimately used only through the induced PTA overlap-reduction function (ORF), we select λ by requiring the ORF to be stable against further increases in regularization. For each trial λ we construct the corresponding ORF matrix $\Gamma_{ij}(\lambda)$ and quantify the change between neighboring values using the off-diagonal relative RMS,

$$r(\lambda_a, \lambda_b) \equiv \left[\frac{\sum_{i<j} (\Gamma_{ij}(\lambda_a) - \Gamma_{ij}(\lambda_b))^2}{\sum_{i<j} \Gamma_{ij}^2(\lambda_b)} \right]^{1/2}, \quad (\text{A4})$$

together with the off-diagonal Pearson correlation coefficient $\rho(\lambda_a, \lambda_b)$. We then choose the smallest λ lying on the stability plateau, i.e. satisfying $r(\lambda, \lambda_{\text{next}}) \ll 1$ and $\rho(\lambda, \lambda_{\text{next}}) \simeq 1$ for subsequent λ values. In our scan we find that $\lambda \simeq 1$ is the onset of this plateau; we therefore adopt $\lambda = 1$ for the fiducial analysis. We verified that varying λ within the plateau (e.g. $\lambda \in [1, 2]$) leaves the ORF essentially unchanged.

REFERENCES

- Afzal, A., Agazie, G., Anumalapudi, A., et al. 2023, *The Astrophysical Journal* / 2, 951, L11, doi: [10.3847/2041-8213/acdc91](https://doi.org/10.3847/2041-8213/acdc91)
- Agazie, G., et al. 2023, *Astrophys. J. Lett.*, 956, L3, doi: [10.3847/2041-8213/acf4fd](https://doi.org/10.3847/2041-8213/acf4fd)
- Agazie, G., Anumalapudi, A., Archibald, A. M., et al. 2023, *ApJL*, 952, L37, doi: [10.3847/2041-8213/ace18b](https://doi.org/10.3847/2041-8213/ace18b)
- . 2023a, *ApJL*, 951, L8, doi: [10.3847/2041-8213/acdac6](https://doi.org/10.3847/2041-8213/acdac6)
- Agazie, G., Alam, M. F., Anumalapudi, A., et al. 2023b, *ApJL*, 951, L9, doi: [10.3847/2041-8213/acda9a](https://doi.org/10.3847/2041-8213/acda9a)
- Alba, V., & Maldacena, J. 2016, *Journal of High Energy Physics*, 2016, 115, doi: [10.1007/JHEP03\(2016\)115](https://doi.org/10.1007/JHEP03(2016)115)
- Ali-Haïmoud, Y., Smith, T. L., & Mingarelli, C. M. F. 2021, *Phys. Rev. D*, 103, 042009, doi: [10.1103/PhysRevD.103.042009](https://doi.org/10.1103/PhysRevD.103.042009)
- Allen, B., Agarwal, D., Romano, J. D., & Valtolina, S. 2024, *PhRvD*, 110, 123507, doi: [10.1103/PhysRevD.110.123507](https://doi.org/10.1103/PhysRevD.110.123507)
- Alonso, D., Sanchez, J., Slosar, A., & Collaboration, L. D. E. S. 2019, *Monthly Notices of the Royal Astronomical Society*, 484, 4127, doi: [10.1093/mnras/stz093](https://doi.org/10.1093/mnras/stz093)
- Anholm, M., Ballmer, S., Creighton, J. D. E., Price, L. R., & Siemens, X. 2009, *PhRvD*, 79, 084030, doi: [10.1103/PhysRevD.79.084030](https://doi.org/10.1103/PhysRevD.79.084030)
- Arzoumanian, Z., Baker, P. T., Brazier, A., et al. 2021, *ApJ*, 914, 121, doi: [10.3847/1538-4357/abfcd3](https://doi.org/10.3847/1538-4357/abfcd3)
- Bartolo, N., Bertacca, D., Matarrese, S., et al. 2020, *PhRvD*, 102, 023527, doi: [10.1103/PhysRevD.102.023527](https://doi.org/10.1103/PhysRevD.102.023527)
- Bécsy, B., Cornish, N. J., & Kelley, L. Z. 2022, *ApJ*, 941, 119, doi: [10.3847/1538-4357/aca1b2](https://doi.org/10.3847/1538-4357/aca1b2)
- Bi, Y.-C., Wu, Y.-M., Chen, Z.-C., & Huang, Q.-G. 2023, *Sci. China Phys. Mech. Astron.*, 66, 120402, doi: [10.1007/s11433-023-2252-4](https://doi.org/10.1007/s11433-023-2252-4)
- Bilicki, M., Peacock, J. A., Jarrett, T. H., et al. 2014, *Astrophysical Journal Supplement Series*, 210, 9, doi: [10.1088/0067-0049/210/1/9](https://doi.org/10.1088/0067-0049/210/1/9)
- Bunn, E. F., Hoffman, Y., & Silk, J. 1994, *The Astrophysical Journal Letters*, 432, L75, doi: [10.1086/187515](https://doi.org/10.1086/187515)
- Caprini, C., & Figueroa, D. G. 2018, *Classical and Quantum Gravity*, 35, 163001, doi: [10.1088/1361-6382/aac608](https://doi.org/10.1088/1361-6382/aac608)
- Chen, Y., et al. 2026, *Phys. Rev. D*, 113, 043042, doi: [10.1103/czxp-zrd6](https://doi.org/10.1103/czxp-zrd6)
- Chiara Guzzetti, M., Bartolo, N., Liguori, M., & Matarrese, S. 2016, *arXiv e-prints*, arXiv:1605.01615, doi: [10.48550/arXiv.1605.01615](https://doi.org/10.48550/arXiv.1605.01615)
- Cornish, N. J., & Sesana, A. 2013, *Classical and Quantum Gravity*, 30, 224005, doi: [10.1088/0264-9381/30/22/224005](https://doi.org/10.1088/0264-9381/30/22/224005)
- Cornish, N. J., & van Haasteren, R. 2014, *arXiv e-prints*, arXiv:1406.4511, doi: [10.48550/arXiv.1406.4511](https://doi.org/10.48550/arXiv.1406.4511)
- Creighton, J., & Anderson, W. 2011, *Gravitational-Wave Physics and Astronomy: An Introduction to Theory, Experiment and Data Analysis*. (Wiley -VCH Verlag GmbH & Co. KGaA)
- Cusin, G., Pitrou, C., Pijenburg, M., & Sesana, A. 2025, *MNRAS*, 541, 2884, doi: [10.1093/mnras/staf1074](https://doi.org/10.1093/mnras/staf1074)
- Detweiler, S. 1979, *ApJ*, 234, 1100, doi: [10.1086/157593](https://doi.org/10.1086/157593)
- Donoso, E., Li, C., Kauffmann, G., Best, P. N., & Heckman, T. M. 2010, *Monthly Notices of the Royal Astronomical Society*, 407, 1078, doi: [10.1111/j.1365-2966.2010.16907.x](https://doi.org/10.1111/j.1365-2966.2010.16907.x)
- Ellis, J., & Lewicki, M. 2021, *Phys. Rev. Lett.*, 126, 041304, doi: [10.1103/PhysRevLett.126.041304](https://doi.org/10.1103/PhysRevLett.126.041304)

- Ellis, J., & van Haasteren, R. 2019, PTMCMCSampler: Parallel tempering MCMC sampler package written in Python, Astrophysics Source Code Library, record ascl:1912.017. <http://ascl.net/1912.017>
- Ellis, J. A., Vallisneri, M., Taylor, S. R., & Baker, P. T. 2020, ENTERPRISE: Enhanced Numerical Toolbox Enabling a Robust Pulsar Inference Suite, Zenodo, doi: [10.5281/zenodo.4059815](https://doi.org/10.5281/zenodo.4059815)
- EPTA Collaboration, InPTA Collaboration, Antoniadis, J., et al. 2023, *A&A*, 678, A50, doi: [10.1051/0004-6361/202346844](https://doi.org/10.1051/0004-6361/202346844)
- Ferrarese, L., & Merritt, D. 2000, *ApJ*, 539, L9, doi: [10.1086/312838](https://doi.org/10.1086/312838)
- Foster, R. S., & Backer, D. C. 1990, *ApJ*, 361, 300, doi: [10.1086/169195](https://doi.org/10.1086/169195)
- Gair, J., Romano, J. D., Taylor, S., & Mingarelli, C. M. F. 2014, *PhRvD*, 90, 082001, doi: [10.1103/PhysRevD.90.082001](https://doi.org/10.1103/PhysRevD.90.082001)
- Gebhardt, K., et al. 2000, *ApJL*, 539, L13, doi: [10.1086/312840](https://doi.org/10.1086/312840)
- Grunthall, K., Nathan, R. S., Thrane, E., et al. 2024, *Monthly Notices of the Royal Astronomical Society*, 536, 1501, doi: [10.1093/mnras/stae2573](https://doi.org/10.1093/mnras/stae2573)
- Hashiguchi, A., Toba, Y., Ota, N., et al. 2023, *Publications of the Astronomical Society of Japan*, 75, 1246, doi: [10.1093/pasj/psad066](https://doi.org/10.1093/pasj/psad066)
- Hickox, R. C., Myers, A. D., Brodwin, M., et al. 2011, *ApJ*, 731, 117, doi: [10.1088/0004-637X/731/2/117](https://doi.org/10.1088/0004-637X/731/2/117)
- Hivon, E., Gorski, K. M., Netterfield, C. B., et al. 2002, *Astrophys. J.*, 567, 2, doi: [10.1086/338126](https://doi.org/10.1086/338126)
- Hotinli, S. C., Kamionkowski, M., & Jaffe, A. H. 2019, *The Open Journal of Astrophysics*, 2, 8, doi: [10.21105/astro.1904.05348](https://doi.org/10.21105/astro.1904.05348)
- Jaffe, A. H., & Backer, D. C. 2003, *ApJ*, 583, 616, doi: [10.1086/345443](https://doi.org/10.1086/345443)
- Joshi, B. C., Arumugasamy, P., Bagchi, M., et al. 2018, *Journal of Astrophysics and Astronomy*, 39, 51, doi: [10.1007/s12036-018-9549-y](https://doi.org/10.1007/s12036-018-9549-y)
- Konstandin, T., Lemke, A.-M., Mitridate, A., & Perboni, E. 2025, *JCAP*, 04, 059, doi: [10.1088/1475-7516/2025/04/059](https://doi.org/10.1088/1475-7516/2025/04/059)
- Kormendy, J., & Ho, L. C. 2013, *ARA&A*, 51, 511, doi: [10.1146/annurev-astro-082708-101811](https://doi.org/10.1146/annurev-astro-082708-101811)
- Kosowsky, A., Turner, M. S., & Watkins, R. 1992, *Phys. Rev. Lett.*, 69, 2026, doi: [10.1103/PhysRevLett.69.2026](https://doi.org/10.1103/PhysRevLett.69.2026)
- Kramer, M., & Champion, D. J. 2013, *Classical and Quantum Gravity*, 30, 224009, doi: [10.1088/0264-9381/30/22/224009](https://doi.org/10.1088/0264-9381/30/22/224009)
- Lahav, O., Fisher, K. B., Hoffman, Y., Scharf, C. A., & Zaroubi, S. 1994, *The Astrophysical Journal Letters*, 423, L93, doi: [10.1086/187244](https://doi.org/10.1086/187244)
- Lazio, T. J. W. 2013, *Classical and Quantum Gravity*, 30, 224011, doi: [10.1088/0264-9381/30/22/224011](https://doi.org/10.1088/0264-9381/30/22/224011)
- Maggiore, M. 2008, *Gravitational waves: Volume 1: Theory and experiments* (Oxford University Press)
- Manchester, R. N. 2013, *Int. J. Mod. Phys. D*, 22, 1341007, doi: [10.1142/S0218271813410071](https://doi.org/10.1142/S0218271813410071)
- Manchester, R. N., & IPTA. 2013, *Classical and Quantum Gravity*, 30, 224010, doi: [10.1088/0264-9381/30/22/224010](https://doi.org/10.1088/0264-9381/30/22/224010)
- Matthee, J., Naidu, R. P., Kotiwale, G., et al. 2025, *ApJ*, 988, 246, doi: [10.3847/1538-4357/ade886](https://doi.org/10.3847/1538-4357/ade886)
- McLaughlin, M. A. 2013, *Classical and Quantum Gravity*, 30, 224008, doi: [10.1088/0264-9381/30/22/224008](https://doi.org/10.1088/0264-9381/30/22/224008)
- Miles, M. T., Shannon, R. M., Bailes, M., et al. 2023, *MNRAS*, 519, 3976, doi: [10.1093/mnras/stac3644](https://doi.org/10.1093/mnras/stac3644)
- Mingarelli, C. M. F., Sidery, T., Mandel, I., & Vecchio, A. 2013, *Phys. Rev. D*, 88, 062005, doi: [10.1103/PhysRevD.88.062005](https://doi.org/10.1103/PhysRevD.88.062005)
- Mingarelli, C. M. F., Lazio, T. J. W., Sesana, A., et al. 2017, *Nature Astronomy*, 1, 886, doi: [10.1038/s41550-017-0299-6](https://doi.org/10.1038/s41550-017-0299-6)
- Nan, R., Li, D., Jin, C., et al. 2011, *International Journal of Modern Physics D*, 20, 989, doi: [10.1142/S0218271811019335](https://doi.org/10.1142/S0218271811019335)
- Perera, B. B. P., DeCesar, M. E., Demorest, P. B., et al. 2019, *MNRAS*, 490, 4666, doi: [10.1093/mnras/stz2857](https://doi.org/10.1093/mnras/stz2857)
- Phinney, E. S. 2001, *A Practical theorem on gravitational wave backgrounds*, arXiv e-prints
- Ravi, V., Wyithe, J. S. B., Hobbs, G., et al. 2012, *ApJ*, 761, 84, doi: [10.1088/0004-637X/761/2/84](https://doi.org/10.1088/0004-637X/761/2/84)
- Reardon, D. J., Zic, A., Shannon, R. M., et al. 2023, *ApJL*, 951, L6, doi: [10.3847/2041-8213/acdd02](https://doi.org/10.3847/2041-8213/acdd02)
- Reines, A. E., & Volonteri, M. 2015, *The Astrophysical Journal*, 813, 82, doi: [10.1088/0004-637X/813/2/82](https://doi.org/10.1088/0004-637X/813/2/82)
- Sah, M. R., Mukherjee, S., Saeedzadeh, V., et al. 2024, *MNRAS*, 533, 1568, doi: [10.1093/mnras/stae1930](https://doi.org/10.1093/mnras/stae1930)
- Sazhin, M. V. 1978, *Soviet Ast.*, 22, 36
- Semenzato, F., Casey-Clyde, J. A., Mingarelli, C. M. F., et al. 2024, arXiv e-prints, arXiv:2411.00532, doi: [10.48550/arXiv.2411.00532](https://doi.org/10.48550/arXiv.2411.00532)
- Sesana, A. 2013, *Classical and Quantum Gravity*, 30, 244009
- Smits, R., Lorimer, D. R., Kramer, M., et al. 2009, *A&A*, 505, 919, doi: [10.1051/0004-6361/200911939](https://doi.org/10.1051/0004-6361/200911939)
- Szapudi, I., Prunet, S., Pogosyan, D., Szalay, A. S., & Bond, J. R. 2001, *ApJL*, 548, L115, doi: [10.1086/319105](https://doi.org/10.1086/319105)

- Taylor, S. R., & Gair, J. R. 2013, *Phys. Rev. D*, 88, 084001, doi: [10.1103/PhysRevD.88.084001](https://doi.org/10.1103/PhysRevD.88.084001)
- Taylor, S. R., van Haasteren, R., & Sesana, A. 2020, *PhRvD*, 102, 084039, doi: [10.1103/PhysRevD.102.084039](https://doi.org/10.1103/PhysRevD.102.084039)
- Taylor, S. R., Mingarelli, C. M. F., Gair, J. R., et al. 2015, *PhRvL*, 115, 041101, doi: [10.1103/PhysRevLett.115.041101](https://doi.org/10.1103/PhysRevLett.115.041101)
- The NANOGrav Collaboration. 2025, The NANOGrav 15-Year Data Set (v2.1.0), Zenodo, doi: [10.5281/zenodo.16051178](https://doi.org/10.5281/zenodo.16051178)
- Verbiest, J. P. W., Lentati, L., Hobbs, G., et al. 2016, *Monthly Notices of the Royal Astronomical Society*, 458, 1267, doi: [10.1093/mnras/stw347](https://doi.org/10.1093/mnras/stw347)
- Vielva, P., Martínez-González, E., & Tucci, M. 2006, *Monthly Notices of the Royal Astronomical Society*, 365, 891, doi: [10.1111/j.1365-2966.2005.09764.x](https://doi.org/10.1111/j.1365-2966.2005.09764.x)
- Wake, D. A., Croom, S. M., Sadler, E. M., & Johnston, H. M. 2008, *Monthly Notices of the Royal Astronomical Society*, 391, 1674, doi: [10.1111/j.1365-2966.2008.14039.x](https://doi.org/10.1111/j.1365-2966.2008.14039.x)
- Wang, Y., & Mohanty, S. D. 2017, *PhRvL*, 118, 151104, doi: [10.1103/PhysRevLett.118.151104](https://doi.org/10.1103/PhysRevLett.118.151104)
- Xu, H., Chen, S., Guo, Y., et al. 2023, *Research in Astronomy and Astrophysics*, 23, 075024, doi: [10.1088/1674-4527/acdfa5](https://doi.org/10.1088/1674-4527/acdfa5)
- Yang, Q., Guo, X., Cao, Z., Shao, X., & Yuan, X. 2025, *ApJ*, 989, 157, doi: [10.3847/1538-4357/aded02](https://doi.org/10.3847/1538-4357/aded02)
- Zaroubi, S., Hoffman, Y., Fisher, K. B., & Lahav, O. 1995, *The Astrophysical Journal*, 449, 446, doi: [10.1086/176070](https://doi.org/10.1086/176070)